Evidence for hidden quadrupolar fluctuations behind the octupole order in $Ce_{0.7}La_{0.3}B_6$ from resonant x-ray diffraction in magnetic fields

Takeshi Matsumura,[1,2,*] Shinji Michimura,[3] Toshiya Inami,[4] Toru Otsubo,[1] Hiroshi Tanida,[1] Fumitoshi Iga,[5] and Masafumi Sera[1,2]

[1]*Department of Quantum Matter, AdSM, Hiroshima University, Higashi-Hiroshima 739-8530, Japan*
[2]*Institute for Advanced Materials Research, Hiroshima University, Higashi-Hiroshima 739-8530, Japan*
[3]*Department of Physics, Faculty of Science, Saitama University, Saitama 338-8570, Japan*
[4]*Condensed Matter Science Division, Japan Atomic Energy Agency, Sayo, Hyogo 679-5148, Japan*
[5]*Faculty of Science, Ibaraki University, Mito, Ibaraki 310-8512, Japan*

(Received 16 September 2012; revised manuscript received 6 January 2014; published 24 January 2014)

The multipole ordered phase in $Ce_{0.7}La_{0.3}B_6$, emerging below 1.5 K and named phase IV, has been studied by resonant x-ray diffraction in magnetic fields. By utilizing diamond x-ray phase plates to rotate the incident linear polarization and a conventional crystal analyzer system, full linear polarization analysis has been performed to identify the order parameters. The analysis shows that the Γ_{5g} (O_{yz}, O_{zx}, O_{xy}) quadrupoles are more induced by the field than the Γ_{3g} (O_{20} and O_{22}) quadrupoles on the Γ_{5u} (T^{β}_{x+y+z}) antiferro-octupole order in phase IV. The problem is that this result is contradictory to a mean-field calculation, which inevitably gives the Γ_{3g} quadrupole as the main induced moment. This result indicates that the Γ_{5g} quadrupole order is close in energy. We consider that a large fluctuation of the Γ_{5g} quadrupole is hidden behind the primary ordering of the Γ_{5u} octupole and that the multipolar fluctuation significantly affects the ordering phenomenon.

DOI: 10.1103/PhysRevB.89.014422 PACS number(s): 71.27.+a, 61.05.cp, 75.25.Dk

I. INTRODUCTION

A rich variety of electronic ordered phases in f electron systems has attracted long-standing interest, where one of the focal points in recent years is on the role of the higher rank multipole moments as a manifestation of an interplay between spin and unquenched orbital degrees of freedom [1,2]. For example, there are many compounds exhibiting electric quadrupole (rank 2) orderings such as CeB_6, $PrPb_3$, DyB_2C_2, TmTe, UPd_3, etc. [3–7]. Although it is rare, magnetic octupole (rank 3), and even a higher multipole, is considered as the primary order parameter in $Ce_xLa_{1-x}B_6$ ($x < 0.8$) and in NpO_2, respectively [8–12]. These ordered phases have attracted special interest because of the hidden nature of the nondipolar interactions and order parameters. It is also an important viewpoint that the hidden orders can give rise to a characteristic spin exciton mode on the hybridized heavy quasiparticle band as revealed recently in CeB_6 [13,14].

The interionic multipole interaction has its origin in hybridization of the f electrons with the conduction and valence electrons. The Ruderman-Kittel-Kasuya-Yosida (RKKY) interaction in metals and superexchange interaction in insulators are the main mechanisms of the interaction originating in hybridization. Simultaneously, hybridization causes the Kondo effect, which may have a significant effect on the ordering phenomenon, e.g., as in $PrFe_4P_{12}$ [2]. An important theoretical argument in the interionic interaction is that the strength of the multipolar interaction is rank independent [1,15,16]. As a result, the higher rank multipoles can equally be a primary order parameter. This also means that the hidden multipolar interactions, which do not result in actual orderings, are equally important as the primary one because they compete with each other, induce fluctuations, and affect the ordering phenomenon. However, it is usually very difficult to show experimentally the existence of hidden fluctuations of another order parameter. They tend to be excluded from consideration due to a lack of evidence. In this context, it is worth mentioning that the multipolar interaction can affect the dynamical behavior of the system as studied in detail in the magnetic ordered phase of UO_2 [18,19].

The $Ce_xLa_{1-x}B_6$ system provides a typical example in which a wide variety of multipole ordered phases are realized [20–25]. They originate in the Γ_8-quartet crystalline electric field (CEF) ground state of a Ce^{3+} ion, possessing fifteen independent moments up to rank 3. All these moments play important roles in the ordering phenomena [15–17]. The H-T phase diagram of $Ce_{0.7}La_{0.3}B_6$ is shown in Fig. 1. One of the most prominent features is the significant increase in the Γ_{5g} (O_{xy}, O_{yz}, O_{zx}) antiferroquadrupole (AFQ) ordering temperature (T_Q) at low fields. One reason for this behavior is that the interaction between the field-induced Γ_{2u} (T_{xyz}) antiferro-octupole (AFO) stabilizes the Γ_{5g}-AFQ ordered phase [15]. This mechanism has actually been evidenced by resonant x-ray diffraction (RXD) for CeB_6 [27–29]. However, to explain the significant increase in T_Q satisfactorily, it is also essential to consider the strong multipolar fluctuations [30,31].

The unusual phase at low fields (phase IV), which emerges for $x < 0.8$ by La substitution, is now considered a Γ_{5u} (T^{β}) AFO phase. [32] An RXD experiment by Mannix *et al.* and an analysis of the azimuthal-angle dependence, as well as a neutron diffraction experiment, well support the AFO scenario [8–10]. However, this does not simply mean the disappearance of the AFQ interaction as assumed in Ref. [32] because the AFQ phase is easily realized by applying a magnetic field. If we take into account the Γ_{5g}-AFQ interaction, however, it becomes difficult to explain the cusp anomaly in the magnetic susceptibility [33]. Also, it is not explained why the I-II phase boundary, when the phase IV exists at low fields, does not approach to a $T > 0$ point at $H = 0$, which is the

*tmatsu@hiroshima-u.ac.jp

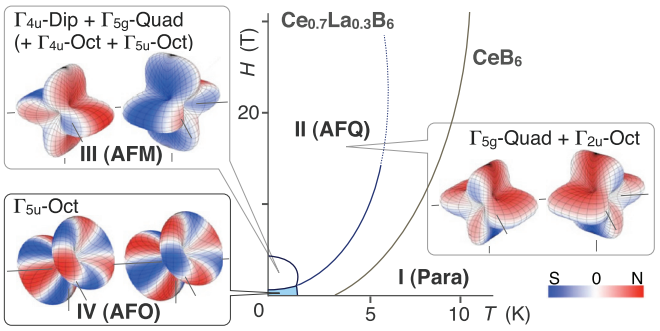

FIG. 1. (Color online) The H-T phase diagram of $Ce_{0.7}La_{0.3}B_6$ for $H \parallel [001]$ and the calculated electric and magnetic charge distributions of the antiferro-type ordered states [26]. The broken line is a speculation. The I-II phase boundary for CeB_6 is also shown for reference.

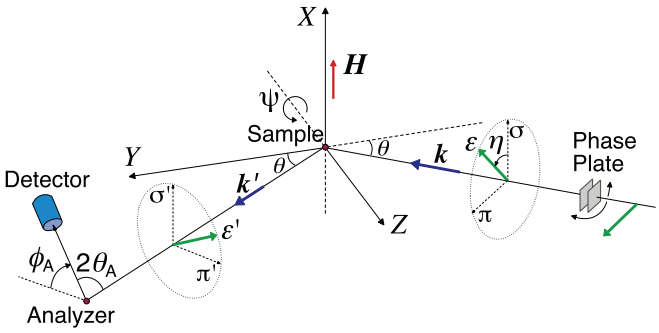

FIG. 2. (Color online) Scattering geometry of the experiment and definitions of the angles.

case in CeB_6 and is expected in a mean-field (MF) model with finite Γ_{5g}-AFQ interaction. This strange behavior of the AFQ phase can be more clearly observed in the phase diagram of $Ce_{0.5}La_{0.5}B_6$ [24]. In the MF scenario, T_Q for the Γ_8 ground state system with quadrupolar degeneracy should always be finite. This means that the I-II phase boundary for $Ce_{0.7}La_{0.3}B_6$ shown in Fig. 1 cannot be reproduced by a normal MF model. It may be necessary to consider an unexpected case where the Γ_8 quartet is somehow split or an unknown effect of multipolar fluctuation involving Γ_{5g}-AFQ and Γ_{5u}-AFO states. Thus there still remain fundamental questions in the phase diagram of $Ce_xLa_{1-x}B_6$.

In the present paper, by taking full advantage of RXD in magnetic fields with full linear polarization analysis (FLPA), we study the field induced multipoles and discuss the hidden AFQ interactions and fluctuations existing behind the primary AFO ordering in $Ce_{0.7}La_{0.3}B_6$. The rest of the paper is organized as follows. After describing the experimental procedure in Sec. II, the results and analysis are presented in Sec. III. In Sec. III A, the nature of the order parameter at zero field is described. We show that the Γ_{5u}-AFO order of $\langle \pm T_x^\beta \pm T_y^\beta \pm T_z^\beta \rangle$ is realized as has been proposed previously. Next, in Sec. III B, we study the field-induced multipoles in phase IV by using the data at both L_2 and L_3 edges, which is the main subject of the paper. It is shown that the main induced moment is the Γ_{5g}-AFQ. In Sec. III C, we describe the results in the Γ_{5g}-AFQ phase at high fields, which has already been well established in the study of CeB_6. Then, using the parameters obtained at ± 4 T, we try to estimate the ordered moment of the Γ_{5u}-AFO at zero field and show that it is reduced from the full moment value. Finally, in Sec. IV, we discuss the field-induced multipoles in phase IV by consulting an MF calculation and point out that the calculation cannot explain the result that the Γ_{5g}-AFQ is strongly induced. The theoretical frameworks of FLPA and RXD are summarized in Appendix.

II. EXPERIMENTAL PROCEDURE

The single crystal sample was grown by a floating-zone method using an image furnace with four xenon lamps [34]. A slice of the sample with a (331) surface with 1.5×2.3 mm^2 in size was prepared by spark cutting. The surface was finally mirror polished.

RXD experiment has been performed at BL22XU in SPring-8. The scattering geometry is shown in Fig. 2. A vertical field 8-T superconducting cryomagnet, equipped with a ^{3}He cryostat insert, was used to achieve a high-field and very-low-temperature environment. The sample was mounted in the ^{3}He cryostat, where the sample can be rotated about the [331] axis. We define $\psi = 0^\circ$ when $\boldsymbol{k} \times \boldsymbol{k}'$ coincides with the $[\bar{1}10]$ direction.

In general, in RXD experiments performed at zero field, the azimuthal-angle (ψ) scan provides extremely valuable information in determining the order parameter [8,9]. This method utilizes the effect that the resonance intensity depends on the geometrical relationship between the order parameter and the incident polarization. In magnetic fields, however, a rotation of the sample simultaneously means a change in the field direction, which changes the ordered state of the system itself. Therefore it is desirable to investigate the system without rotating the sample. One promising method, which we adopt in the present study, is to rotate the incident polarization.

The incident x-ray from the synchrotron source is almost perfectly π polarized with its electric field parallel to the scattering plane. This incident polarization can be rotated to an arbitrary angle η by rotating an x-ray phase plate system about the incident beam [35,36]. In the present experiment, two diamond phase plates, with thickness of 300 μm each, were used to compensate for chromatic aberration [37]. The resultant degree of linear polarization for σ polarization ($\eta = 0^\circ$) was 97.8% at 6.160 keV. For π polarization ($\eta = 90^\circ$), it is equal to that of the initial beam before the phase plate, which is more than 99.9%. The polarization state of the diffracted beam was analyzed using the 220 reflection of an Al crystal around the L_2 edge ($2\theta_A = 89.30^\circ$ at 6.160 keV) and the 200 reflection of a Mo crystal around the L_3 edge ($2\theta_A = 86.95^\circ$ at 5.726 keV).

The lowest temperature in the present experiment was determined to be 1.0 K, though the sensor reading at the lowest temperature was 0.6 K. This is due to the heating by x-ray irradiation. The actual sample temperature under x-ray irradiation was determined by comparing the observed transition fields and temperatures with the phase diagram reported in Ref. [38].

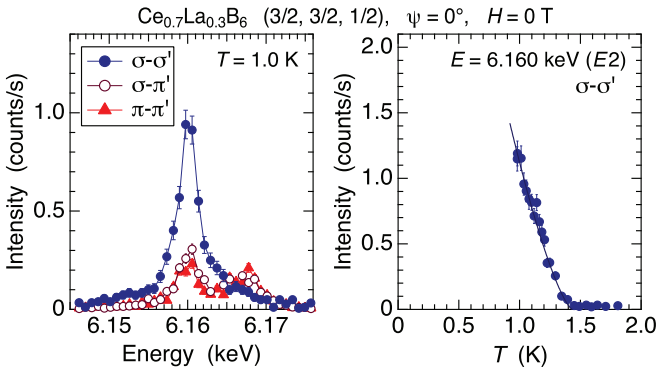

FIG. 3. (Color online) (Left) X-ray energy dependence of the intensity for σ-σ', σ-π', and π-π' channels. (Right) Temperature dependence of the $E2$ resonance intensity at 6.160 keV for the σ-σ' channel. The solid line is a fit to a power law $I \propto |T - T_{\rm IV}|^{2\beta}$ with $\beta = 0.70 \pm 0.1$.

III. RESULTS AND ANALYSIS

A. Order parameter of phase IV at zero field

At the lowest temperature of 1.0 K in phase IV, we successfully detected a resonant peak at $\boldsymbol{k} - \boldsymbol{k}' = (\frac{3}{2}, \frac{3}{2}, \frac{1}{2})$ and $\psi = 0^\circ$ in the L_2-edge experiment. The energy spectra at zero field is shown in Fig. 3, which well reproduces the previous data by Mannix *et al.* reported in Ref. [8] for $(\frac{3}{2}, \frac{3}{2}, \frac{3}{2})$. Only a single resonance peak is observed at 6.160 keV ($E2$) for σ-σ', whereas two peaks are observed at 6.160 keV ($E2$) and at 6.167 keV ($E1$) for σ-π' and π-π'. The $E2$ intensity for σ-σ' disappears at $T_{\rm IV} = 1.4$ K as shown in Fig. 3, indicating that the $E2$ signal reflects the order parameter of phase IV. The critical exponent obtained from the fit to $I \propto |T - T_{\rm IV}|^{2\beta}$ was $\beta = 0.70 \pm 0.1$. Although this value is smaller than 0.99 reported in Ref. [8], it is still larger than a typical value of $\sim$0.35 for three-dimensional systems [5].

To check the order parameter of phase IV at zero field, we performed FLPA for the $E2$ signal at the lowest temperature. Figure 4 shows the $\phi_{\rm A}$ dependencies of the $E2$ intensity at zero field for three different scattering geometries. The observed intensity exhibits a characteristic oscillation, which include similar information to an azimuthal-angle scan. As in the analysis of the azimuthal-angle scan, our strategy is to compare these data with the calculated intensity curves assuming a model ordered structure. As proposed in Ref. [9], we also adopt the Γ_{5u}-AFO order with the order parameter $\langle \pm T_x^\beta \pm T_y^\beta \pm T_z^\beta \rangle$, in which $\langle T_x^\beta \rangle = \langle T_y^\beta \rangle = \langle T_z^\beta \rangle$ is valid. The $(+++)$, $(-++)$, $(+-+)$, and $(++-)$ signs correspond to domains 1, 2, 3, and 4, respectively. In this model, the scattering amplitude operators for domains 1 and 2, at $H = 0$ T and $\hbar\omega = 6.160$ keV (L_2-$E2$), can be written as

$$\hat{F}_1 = \alpha_{E2}^{(3)}(\omega)\left(\hat{G}_{E2}^{T_x^\beta} + \hat{G}_{E2}^{T_y^\beta} + \hat{G}_{E2}^{T_z^\beta}\right)\langle T_x^\beta \rangle, \tag{1a}$$

$$\hat{F}_2 = \alpha_{E2}^{(3)}(\omega)\left(-\hat{G}_{E2}^{T_x^\beta} + \hat{G}_{E2}^{T_y^\beta} + \hat{G}_{E2}^{T_z^\beta}\right)\langle T_x^\beta \rangle, \tag{1b}$$

where $\alpha_{E2}^{(3)}(\omega)$ represents the rank-3 spectral function for the $E2$ resonance at $\hbar\omega = 6.160$ keV (see Appendix B for detailed formalism).

From the $\hat{G}$ matrices listed in Appendix B, we see that $\hat{F}_1$ gives only unrotated σ-σ' and π-π' scatterings, whereas $\hat{F}_2$ gives only σ-π' and π-σ' scatterings. With respect to domains 3 and 4, the intensities are equal to those of domains 2 and 1, respectively. The calculated intensity curves in Fig. 4 assume equal populations of the four domains, i.e., the intensities from each domain are calculated independently and are simply summed up. As shown by the solid lines, which were obtained by putting $|\alpha_{E2}^{(3)}|\langle T_x^\beta \rangle = 2.6$ in Eq. (1), the data are well reproduced by this AFO model, except the unknown discrepancy around $\phi_{\rm A} = 30^\circ$ for $\eta = 0^\circ$ at $(\frac{3}{2}, \frac{3}{2}, \frac{3}{2})$. The possibility of an AFQ contribution as suggested in Refs. [39] and [40] can be ruled out because the AFQ models hardly explain the present result of FLPA. Thus, also from the FLPA approach, the order parameter of phase IV can be concluded as $\langle \pm T_x^\beta \pm T_y^\beta \pm T_z^\beta \rangle$.

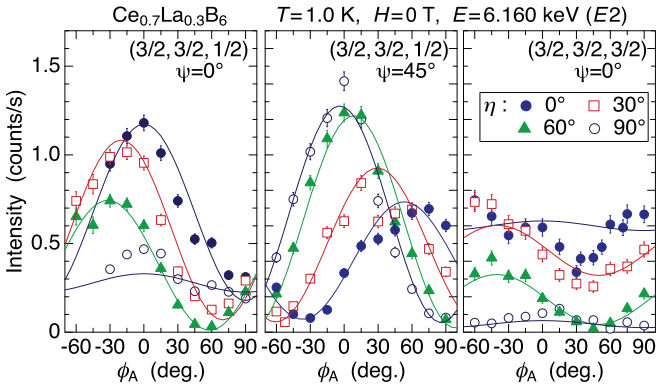

FIG. 4. (Color online) $\phi_{\rm A}$ dependencies of the $E2$ intensity at zero field in phase IV. The incident polarization angle η is fixed and $\phi_{\rm A}$ is scanned. Solid lines show the calculated intensity curves assuming the Γ_{5u}-type AFO order of $\langle \pm T_x^\beta \pm T_y^\beta \pm T_z^\beta \rangle$ with four equal domain populations.

B. Field-induced multipoles in phase IV

1. L_2 edge

The main subject of our study is the magnetic field effect on the AFO order of phase IV. Figure 5 shows the H dependencies of the $E2$ intensity for σ-σ' ($\eta = 0^\circ$, $\phi_A = 0^\circ$) and π-σ' ($\eta = 90^\circ$, $\phi_A = 0^\circ$) channels for $H \parallel [\bar{1}10]$. The field direction is reversed to investigate the interference effect between odd and even rank multipoles, which provides us with a chance to extract field-induced multipoles with different parities [27–29]. Remarkably, the σ-σ' intensity exhibits a significant asymmetry in phase IV on the field reversal. By contrast, the π-σ' intensity smoothly decreases with increasing field and seems to exhibit a quadratic H dependence in phase IV. To identify the order parameter, we performed a FLPA measurement at $H = \pm 1$ T, the result of which is shown in Fig. 6. It is emphasized that investigation of the order parameter by FLPA is especially powerful in magnetic fields, where the azimuthal scan does not make sense.

To analyze the data, we need to assume a model order parameter. From symmetry arguments, and also from an MF calculation, it is possible to predict what kind of multipoles

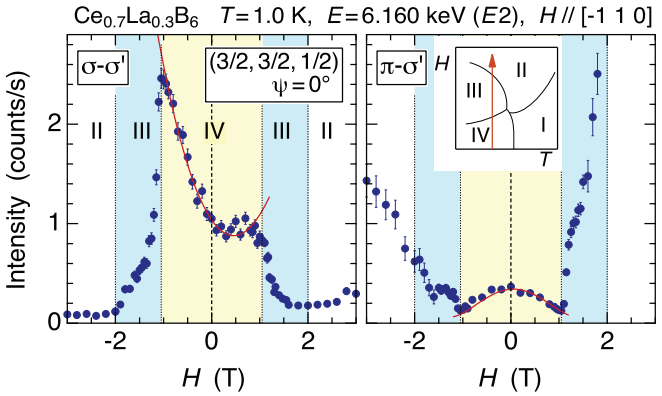

FIG. 5. (Color online) Magnetic-field dependencies of the $E2$ intensity for σ-σ' and π-σ' channels. The solid lines are the calculations described in the text. Inset in the right panel illustrates the H-T phase diagram for $H \parallel [\bar{1}10]$ and the arrow represents the sweep line.

are induced in the AFO phase, which is summarized in Table I. These field-induced moments give rise to additional scattering amplitudes to that of Γ_{5u}-AFO at zero field. It is noted here that, as shown in Fig. 7, the energy spectra at $H = \pm 1$ T for σ-σ' remain single peaked at $E2$ and the interference with the $E1$ resonance can be neglected. Therefore the total scattering amplitude $\hat{F}_i$ for domain-i ($i = 1 \sim 4$) at $H = \pm 1$ T and $\hbar\omega =$ 6.160 keV (L_2-$E2$) can be written as

$$\hat{F}_{i,\pm} = \sum_{\nu,\mu} \alpha^{(\nu)}_{E2}(\omega)\hat{G}^{(\nu)}_{E2,\mu}\langle z^{(\nu)}_{\mu}\rangle_{\pm}. \qquad (2)$$

We take into account all the moments listed in Table I. Since domains 1 and 4, as well as domains 2 and 3, give the same intensity, we give a description only for domains 1 and 2 hereafter.

We analyze the data by treating $\alpha^{(\nu)}_{E2}(\omega)\langle z^{(\nu)}_{\mu}\rangle_{\pm}$ as experimental parameters, which are listed in Table II. Here, the Γ_{5u}-AFO order parameter is assumed to be constant in phase IV. This is roughly consistent with the fact that the transition temperature $T_{\rm IV}$ changes little by the field [20,22,38]. The

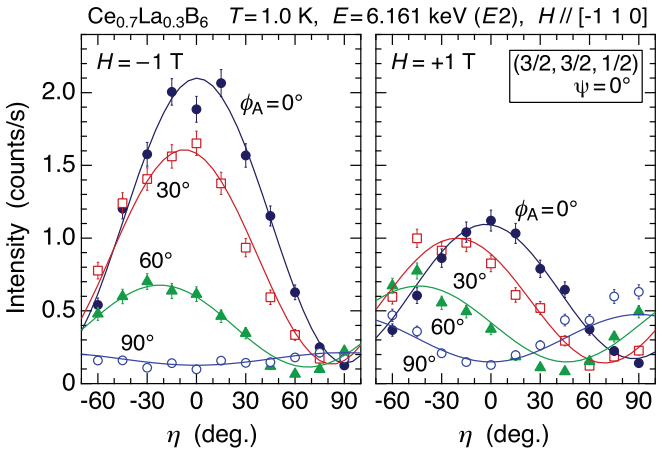

FIG. 6. (Color online) Incident polarization dependencies of the $E2$ intensity at $H = \pm 1$ T. $\phi_{\rm A}$ is fixed and the incident polarization angle η is scanned. Solid lines are the calculations.

TABLE I. Magnetic-field-induced antiferro-moments in the Γ_{5u}-AFO phase for $H \parallel [\bar{1}10]$, which are deduced from symmetry analysis [15], as well as from an MF calculation.

Rank	Irrep	Domains 1 and 4	Domains 2 and 3
3	Γ_{5u}	$T^{\beta}_x + T^{\beta}_y \pm T^{\beta}_z$	$\mp T^{\beta}_x \pm T^{\beta}_y + T^{\beta}_z$
1	Γ_{4u}	$J_x - J_y$	$J_x + J_y$
2	Γ_{3g}	O_{20}	O_{22}
	Γ_{5g}	$O_{yz} + O_{zx}$, O_{xy}	$O_{yz} + O_{zx}$
3	Γ_{4u}	$T^{\alpha}_x - T^{\alpha}_y$	$T^{\alpha}_x + T^{\alpha}_y$

domain population is also assumed stable in the field of 1 T. With respect to the field-induced moments, we impose a condition that the quadrupole moments change sign with the field reversal and the octupole moments do not. This is an important characteristic of the AFO ordered phase as demonstrated by the MF model calculation later. We note that since we can construct an infinite number of numerical (unphysical) solutions to fit the data in Fig. 6, we selected a physically plausible set of parameters that is consistent as much as possible with the MF calculation (with respect to the signs and the relative ratios). The rank-1 and rank-4 contributions were neglected because they are considered to be small at ± 1 T.

Although the number of parameters seems large, the main effect is actually dominated by two factors. Firstly, the significant field-reversal asymmetry for σ-σ' and π-π', the most important part of the data, is caused by the interference between the Γ_{5u}-AFO and the field induced $(\Gamma_{3g} + \Gamma_{5g})$-AFQ in domain 1. The Γ_{4u}-AFO in domain 1 has only a marginal effect, and can even be neglected. Secondly, the symmetric H dependence for σ-π' and π-σ' is due to the cancellation of the scattering amplitude of Γ_{5u}-AFO by that of the Γ_{4u}-AFO in domain 2. It is again noted that the σ-σ' and π-π' intensities arise from domain 1, and π-σ' and σ-π' intensities from domain 2, respectively, which can be seen from the $\hat{G}$ factor listed in Appendix B. The calculated intensities are shown by the solid lines in Fig. 6, which reproduce the data very well. The $\langle T^{\alpha}_z\rangle$-AFO in domain 2, which is not expected to appear in Table I, is supposed to be due to a small mixing of the phase III order parameter. Finally, the $\langle O_{22}\rangle$-AFQ and

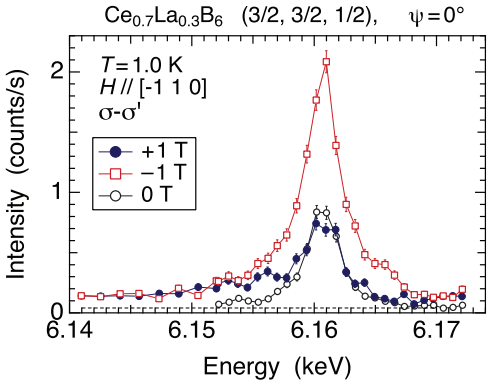

FIG. 7. (Color online) X-ray energy dependencies of the intensity for σ-σ' at $H = \pm 1$ and 0 T.

TABLE II. The parameters in Eq. (2) to explain the result of Fig. 6. We write $\alpha_{E2}^{(\nu)}$ as $|\alpha_{E2}^{(\nu)}|e^{i\delta_2^{(\nu)}}$ and the phase difference $\delta_2^{(2)} - \delta_2^{(3)}$ is set to -0.15π, which best explains the data. It is noted that in domain 1, $\langle T_x^\beta\rangle = \langle T_y^\beta\rangle = \langle T_z^\beta\rangle$, $\langle T_x^\alpha\rangle = -\langle T_y^\alpha\rangle$, and $\langle O_{yz}\rangle = \langle O_{zx}\rangle$ is satisfied, and in domain 2, $-\langle T_x^\beta\rangle = \langle T_y^\beta\rangle = \langle T_z^\beta\rangle$, $\langle T_x^\alpha\rangle = \langle T_y^\alpha\rangle$, and $\langle O_{yz}\rangle = \langle O_{zx}\rangle$ is satisfied.

Domains 1 and 4	Irrep	0 T	+1 T	−1 T
$\lvert\alpha_{E2}^{(3)}\rvert\langle T_x^\beta\rangle$	Γ_{5u}	2.6	2.6	2.6
$\lvert\alpha_{E2}^{(3)}\rvert\langle T_x^\alpha\rangle$	Γ_{4u}	0	-0.5 ± 0.5	-0.5 ± 0.5
$\lvert\alpha_{E2}^{(2)}\rvert\langle O_{20}\rangle$	Γ_{3g}	0	-1.6 ± 0.5	1.6 ± 0.5
$\lvert\alpha_{E2}^{(2)}\rvert\langle O_{yz}\rangle$	Γ_{5g}	0	-1.4 ± 0.5	1.4 ± 0.5
$\lvert\alpha_{E2}^{(2)}\rvert\langle O_{xy}\rangle$	Γ_{5g}	0	3.0 ± 0.5	-3.0 ± 0.5
Domains 2 and 3				
$\lvert\alpha_{E2}^{(3)}\rvert\langle T_x^\beta\rangle$	Γ_{5u}	−2.6	−2.6	−2.6
$\lvert\alpha_{E2}^{(3)}\rvert\langle T_x^\alpha\rangle$	Γ_{4u}	0	0.5 ± 0.2	0.5 ± 0.2
$\lvert\alpha_{E2}^{(3)}\rvert\langle T_z^\alpha\rangle$	Γ_{4u}	0	0.8 ± 0.2	0.8 ± 0.2
$\lvert\alpha_{E2}^{(2)}\rvert\langle O_{22}\rangle$	Γ_{3g}	0	1 ± 1.5	-1 ± 1.5
$\lvert\alpha_{E2}^{(2)}\rvert\langle O_{yz}\rangle$	Γ_{5g}	0	-1 ± 1	1 ± 1

$\langle O_{yz} + O_{zx}\rangle$-AFQ in domain 2, which are listed in Table II with very large error bars, have little effect on the fitting result and will be excluded from the discussion later.

The peculiar H dependencies in Fig. 5 can also be explained by considering that the field-induced AFQ and AFO moments have linear and quadratic dependencies with H, respectively, which will be demonstrated by the MF calculation later. In this case, the intensity for the ε-ε' ($\varepsilon = \sigma$ or π) channel can be written as

$$I_{\varepsilon\varepsilon'}(H) \propto \left|F_{5u,\varepsilon\varepsilon'}^{(3)} + F_{4u,\varepsilon\varepsilon'}^{(3)}H^2 + \left(F_{3g,\varepsilon\varepsilon'}^{(2)} + F_{5g,\varepsilon\varepsilon'}^{(2)}\right)H\right|^2, \quad (3)$$

where $F_{\gamma,\varepsilon\varepsilon'}^{(\nu)} = \sum_{\mu\in\gamma}\alpha_{E2}^{(\nu)}(\omega)G_{E2,\mu,\varepsilon\varepsilon'}^{(\nu)}\langle z_\mu^{(\nu)}\rangle$ represents the ε-ε' scattering factor at $\hbar\omega = 6.160$ keV (L_2-$E2$) for the order parameter $\langle z_\mu^{(\nu)}\rangle$ at $H = 1$ T. The H dependencies for σ-σ' and π-σ' are well explained as shown by the solid lines in Fig. 5. As described above, the strong asymmetry in $I_{\sigma\sigma'}(H)$ is due to the interference between $F_{5u,\sigma\sigma'}^{(3)}$ and $(F_{3g,\sigma\sigma'}^{(2)} + F_{5g,\sigma\sigma'}^{(2)})$ in domain 1, and the symmetric decrease in $I_{\pi\sigma'}(H)$ is due to the cancellation of $F_{5u,\pi\sigma'}^{(3)}$ by $F_{4u,\pi\sigma'}^{(3)}$ in domain 2.

The most important piece of information obtained in Table II is that the values for Γ_{5g}-AFQ and Γ_{3g}-AFQ in domain 1 are of the same order. If we take into account the fundamental difference in the full moment between Γ_{3g} and Γ_{5g} quadrupoles in the Γ_8 CEF ground state, i.e., the fact that $\langle\Gamma_8|O_{\Gamma_3}|\Gamma_8\rangle = 4$ is four times larger than $\langle\Gamma_8|O_{\Gamma_5}|\Gamma_8\rangle = 1$, the same order of magnitude obtained in Table II indicates that the Γ_{5g}-AFQ is much more induced than the Γ_{3g}-AFQ as compared with the full moment value.

2. L_3 edge

Figure 8 shows the H dependencies of the resonant intensity at the L_3 edge. No significant intensity above background was found at 0 T, where the signal from the Γ_{5u} (T^β) AFO order should exist as was detected at the L_2 edge. This is considered to be due to the smaller $|\alpha_{E2}^{(3)}|$ for the L_3 edge

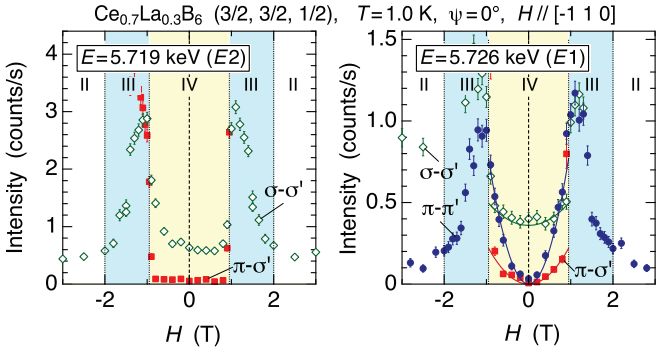

FIG. 8. (Color online) Magnetic-field dependencies of the $E1$ and $E2$ intensities for the π-π', π-σ', and σ-σ' channels at the L_3 edge. The background level for σ-σ' is ∼0.4 counts/s.

than that for the L_2 edge. By contrast, a magnetic field effect was clearly observed, especially for π-π' at $E1$. The data show that the π-π' intensity increases quadratically with H in phase IV. The same behavior is weakly observed also for π-σ'. With respect to σ-σ', an asymmetric intensity on the field reversal is weakly observed at the $E2$ energy, which is likely to reflect the interference between the rank-2 and rank-3 moments as observed in the L_2-edge result of Fig. 5. However, since the relevant intensity is weak and the interference with the nonresonant scattering described next should also be taken into account, further discussion on this asymmetry is difficult.

On entering phase III above 1 T, the σ-σ' intensity is overwhelmed by the nonresonant signal as shown in Fig. 9. This is due to the Thomson scattering from the aspherical charge distribution of the AFQ order in phase III [41,42]. The nonresonant signal is also observed in the L_2-edge experiment in Fig. 7 at $H = \pm 1$ T. The small jump at 1.5 T in Fig. 8, clearly observed at $E2$ energy for σ-σ', may be due to the transition to phase III' [43]. With respect to π-π', the energy dependence in Fig. 9 is characterized by the resonance at $E1$. The contribution from the nonresonant scattering is $|\cos 2\theta|^2 (\simeq 0.12)$ times the σ-σ' intensity, and can be neglected in the $E1$ resonance in Fig. 8.

Let us analyze the H dependencies of the $E1$ intensity. Among the field induced moments shown in Table I, the dipole

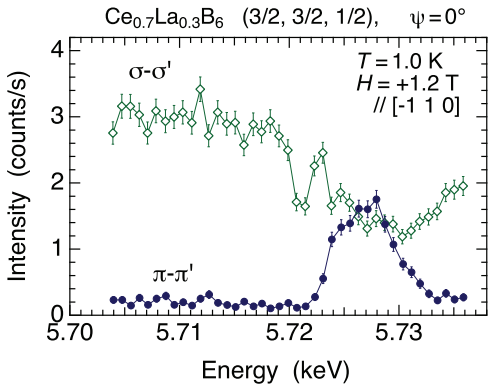

FIG. 9. (Color online) X-ray energy dependencies of the intensity at 1.2 T for σ-σ' and π-π'.

TABLE III. The parameters in Eq. (4) to explain the H dependencies of the $E1$ resonant intensity in Fig. 8.

Domains 1 and 4	$\lvert\alpha^{(2)}_{E1}\rvert\langle O_{20}\rangle$	$\lvert\alpha^{(2)}_{E1}\rvert\langle O_{yz}\rangle$	$\lvert\alpha^{(2)}_{E1}\rvert\langle O_{xy}\rangle$
	-1.6	-1.1	1.6
Domains 2 and 3	$\lvert\alpha^{(2)}_{E1}\rvert\langle O_{22}\rangle$	$\lvert\alpha^{(2)}_{E1}\rvert\langle O_{yz}\rangle$	
	1.2	-1.1	

and quadrupole moments contribute to the $E1$ resonance. However, the $E1$ intensity here at the L_3 edge is dominated by the rank-2 signal, and the rank-1 contribution can be neglected. This is reasoned by the fact that $|\alpha^{(2)}_{E1}|$ is much larger than $|\alpha^{(1)}_{E1}|$ at the L_3 edge, and also by the symmetric H dependence in phase IV indicating little interference effect between rank-1 and rank-2 scatterings. This treatment is justified by the previous study on CeB_6 at the L_3 edge [29]. Therefore the field-dependent resonant structure factors for domains 1 and 2, at $\hbar\omega = 5.726$ keV (L_3-$E1$), can be written as

$$\hat{F}_1(H) = \lvert\alpha^{(2)}_{E1}\rvert e^{i\delta^{(2)}_1}\big[\hat{G}^{O_{20}}_{E1}\langle O_{20}\rangle + \big(\hat{G}^{O_{yz}}_{E1} + \hat{G}^{O_{zx}}_{E1}\big)\langle O_{yz}\rangle + \hat{G}^{O_{xy}}_{E1}\langle O_{xy}\rangle\big]H, \quad (4a)$$

$$\hat{F}_2(H) = \lvert\alpha^{(2)}_{E1}\rvert e^{i\delta^{(2)}_1}\big[\hat{G}^{O_{22}}_{E1}\langle O_{22}\rangle + \big(\hat{G}^{O_{yz}}_{E1} + \hat{G}^{O_{zx}}_{E1}\big)\langle O_{yz}\rangle\big]H. \quad (4b)$$

By using the parameters listed in Table III, the experimental results can be well reproduced, which are shown by the solid lines in Fig. 8. Since these parameters could not be determined uniquely, the physically plausible ones were selected so that they are consistent as much as possible with Table II and also with the result of MF calculation described later. The AFQ moments of domains 2 and 3 are also deduced here, which was not obtained in the L_2-edge experiment due to the weak contribution. The resultant parameters in Table III, the same order of magnitude for the Γ_{5g}-AFQ and Γ_{3g}-AFQ, again show that the Γ_{5g}-AFQ is much more induced than the Γ_{3g}-AFQ, which cannot be explained by the MF model described later.

C. AFQ phase at high fields

1. L_2 edge

The AFO order of phase IV exhibits a first-order transition to the AFM phase III at $|H| = 1$ T for $H \parallel [\bar{1}10]$. This behavior can be observed in Fig. 5 as the sudden decrease and increase intensity for σ-σ' and π-σ', respectively. The σ-σ' intensity finally disappears on entering the AFQ phase II, and the resonant signal in the AFQ phase is dominated by the π-σ' scattering. In Fig. 10 the significant increase in the π-σ' intensity on entering the AFM and AFQ phases are demonstrated both for $E1$ and $E2$ resonances at the L_2 edge.

The ordered structure of the multipole moments in the AFQ phase has been well established in CeB_6. For $H \parallel [\bar{1}10]$, antiferro-type orderings of $\langle J_z\rangle$, $\langle O_{yz} - O_{zx}\rangle$, and $\langle T_{xyz}\rangle$ are induced by the field and a single domain state is formed [29]. The same is expected in the AFQ phase of $Ce_{0.7}La_{0.3}B_6$. If

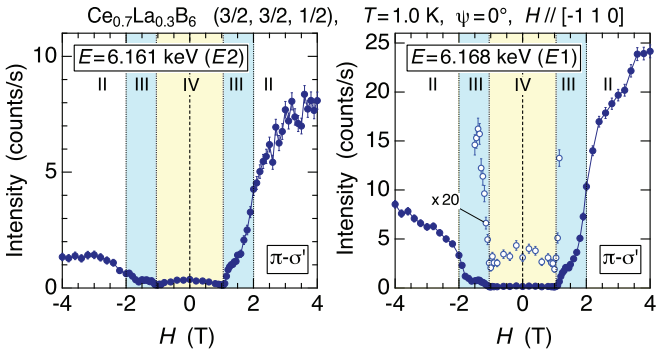

FIG. 10. (Color online) Magnetic-field dependence of the $E2$ and $E1$ intensities for the π-σ' channel.

we perform FLPA and if we could deduce the parameters corresponding to these moments in the AFQ phase, the values could be directly compared with those of Table II, which will be of great significance. In particular, the $\langle T_{xyz}\rangle$-AFO moment in the AFQ phase, at 4 T, for example, can be a good measure of the AFO moment because it is almost saturated and can be used to evaluate the value of the $\langle T^{\beta}\rangle$-AFO moment in Table II.

In Fig. 11, the energy spectra for π-σ' at $H = \pm 4$ T are shown. A significant difference in intensity by the field reversal is observed, indicating a strong interference between the induced moments described above. However, the spectra are much different from those of the L_3-edge experiment reported for CeB_6 [27,29]. Since the order parameters are expected to be the same, this difference can be attributed to the difference in the spectral functions of the L_2 and the L_3 edges.

Figures 12 and 13 show the results of FLPA at $E1$ and $E2$ energies, respectively. With respect to the $E1$ resonance, only the dipole and quadrupole moments are involved. In the field-induced AFQ phase of $Ce_{0.7}La_{0.3}B_6$, the AFQ moment is considered to change sign by the field reversal because it is connected to the ordered state of phase IV in which the AFQ moments change sign and the AFM moments do not. Thus the scattering amplitude operator at $H = \pm 4$ T and $\hbar\omega = 6.168$ keV

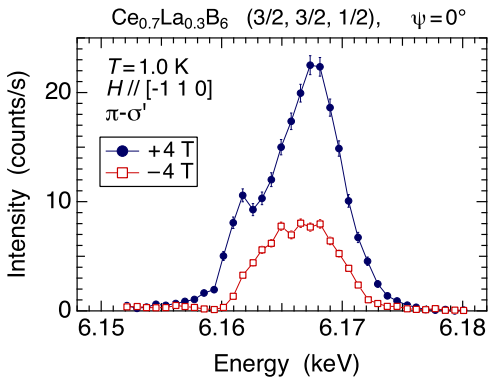

FIG. 11. (Color online) Magnetic-field dependence of the $E2$ and $E1$ intensities for the π-σ' channel.

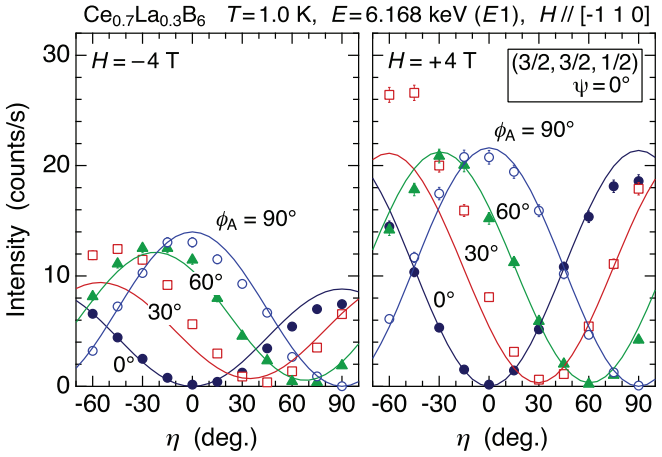

FIG. 12. (Color online) Incident polarization dependencies of the $E1$ intensity at $H = \pm 4$ T. Solid lines are the calculations.

(L_2-$E1$) can be written as

$$\hat{F}_{\pm} = |\alpha_{E1}^{(1)}| e^{i\delta_1^{(1)}} \hat{G}_{E1}^{J_z} \langle J_z \rangle \pm |\alpha_{E1}^{(2)}| e^{i\delta_1^{(2)}} \left(\hat{G}_{E1}^{O_{yz}} - \hat{G}_{E1}^{O_{zx}} \right) \langle O_{yz} \rangle. \tag{5}$$

In this case, the number of parameters is small, which makes the unique determination possible. By using the fitting parameters $|\alpha_{E1}^{(1)}|\langle J_z \rangle = 4.3 \pm 0.2$, $|\alpha_{E1}^{(2)}|\langle O_{yz} \rangle = 2.8 \pm 0.5$, and $\delta_1^{(1)} - \delta_2^{(1)} = (-0.14 \pm 0.05)\pi$, the data can be well reproduced as shown by the solid lines in Fig. 12. Using these parameters, for π-σ', $I_{\pi\sigma'}(+4\ \mathrm{T}) = 15.1 + 6.3 = 21.4$ and $I_{\pi\sigma'}(-4\ \mathrm{T}) = 15.1 - 6.3 = 8.8$ are calculated, and the average value of 15.1 is divided into $I_{\mathrm{dip}} + I_{\mathrm{quad}} = 9.2 + 5.9$, indicating that the dipolar contribution is larger than the quadrupolar contribution. This result is opposite to that of the L_3 edge [29] where the dipolar contribution is very small. This is due to the difference in the spectral functions.

With respect to the $E2$ resonance, since the tail of the $E1$ spectrum seems to have a significant intensity at the $E2$ energy, it is necessary to take into account the interference with the $E1$ resonance. Then, the scattering amplitude operator at $H = \pm 4$ T

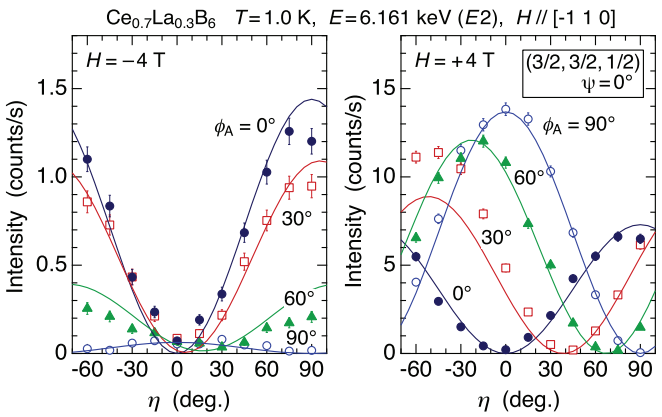

FIG. 13. (Color online) Incident polarization dependencies of the $E2$ intensity at $H = \pm 4$ T. Solid lines are the calculations.

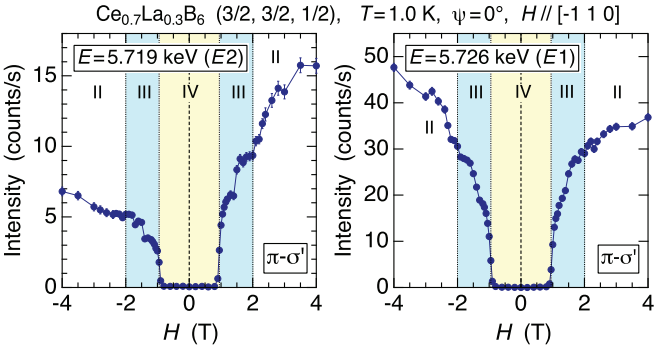

FIG. 14. (Color online) Magnetic-field dependence of the $E2$ and $E1$ intensities for the π-σ' channel.

and $\hbar\omega = 6.161$ keV (L_2-$E2$) can be written as

$$\begin{aligned}\hat{F}_{\pm} = {} & |\alpha_{E1}^{(1)}| e^{i\delta_1^{(1)}} \hat{G}_{E1}^{J_z} \langle J_z \rangle \pm |\alpha_{E1}^{(2)}| e^{i\delta_1^{(2)}} \left(\hat{G}_{E1}^{O_{yz}} - \hat{G}_{E1}^{O_{zx}} \right) \langle O_{yz} \rangle \\ & + |\alpha_{E2}^{(1)}| e^{i\delta_2^{(1)}} \hat{G}_{E2}^{J_z} \langle J_z \rangle \pm |\alpha_{E2}^{(2)}| e^{i\delta_2^{(2)}} \left(\hat{G}_{E2}^{O_{yz}} - \hat{G}_{E1}^{O_{zx}} \right) \langle O_{yz} \rangle \\ & + |\alpha_{E2}^{(3)}| e^{i\delta_2^{(3)}} \left(\hat{G}_{E2}^{T_z^{\alpha}} \langle T_z^{\alpha} \rangle + \hat{G}_{E2}^{T_{xyz}} \langle T_{xyz} \rangle \right). \end{aligned} \tag{6}$$

The problem of this model is that the physically plausible parameters cannot be obtained uniquely. The data in Fig. 13 can be reproduced well by controlling $|\alpha_{E1}^{(1)}|\langle J_z \rangle$, $|\alpha_{E2}^{(1)}|\langle J_z \rangle$, and $|\alpha_{E2}^{(2)}|\langle O_{yz} \rangle$ for any $|\alpha_{E2}^{(3)}|\langle T_{xyz} \rangle$ values from 0 to 20, one of which is shown by the solid lines in Fig. 13. Therefore, unfortunately, $|\alpha_{E2}^{(3)}|\langle T_{xyz} \rangle$ cannot be determined from these data.

2. L_3 edge

Also in the L_3 edge, the σ-σ' and π-π' intensities finally disappear in the AFQ phase, and the resonant signal is dominated by the π-σ' and σ-π' scatterings. Figure 14 demonstrates the jump in intensity at the first-order transition at ± 1 T and the significant increase in intensity in phases III and II. It is noted that the intensity in phase IV is not zero, which is shown in Fig. 8. The energy spectra at ± 4 T is not shown here because they are basically the same as those of CeB_6, which has been reported previously [27,29].

Figures 15 and 16 show the results of FLPA at $E1$ and $E2$ energies, respectively. The scattering amplitude operator for the $E1$ resonance at ± 4 T can be written as Eq. (5), where we use the spectral functions for the L_3 edge. In this case as well, the parameters can be determined uniquely, which are $|\alpha_{E1}^{(1)}|\langle J_z \rangle = 0.7 \pm 0.3$, $|\alpha_{E1}^{(2)}|\langle O_{yz} \rangle = 6.7 \pm 0.3$, and $\delta_1^{(1)} - \delta_1^{(2)} = (0.8 \pm 0.05)\pi$. As shown by the solid lines in Fig. 15, the data are well reproduced by the calculation. Using these parameters, for π-σ', $I_{\pi\sigma'}(+4\ \mathrm{T}) = 36.47 + 3.27 = 39.74$ and $I_{\pi\sigma'}(-4\ \mathrm{T}) = 36.47 - 3.27 = 33.2$. The average value of 36.47 is divided into $I_{\mathrm{dip}} + I_{\mathrm{quad}} = 0.21 + 36.26$, indicating that the quadrupolar contribution is much larger than the dipolar one. This result is consistent with the previous report on CeB_6 [29]. The difference between the L_2 and L_3 edges, $I_{\pi\sigma'}(+4\ \mathrm{T}) > I_{\pi\sigma'}(-4\ \mathrm{T})$ at the L_2 edge, whereas $I_{\pi\sigma'}(+4\ \mathrm{T}) < I_{\pi\sigma'}(-4\ \mathrm{T})$ at the L_3 edge, is due to the difference in the spectral functions between the two edges.

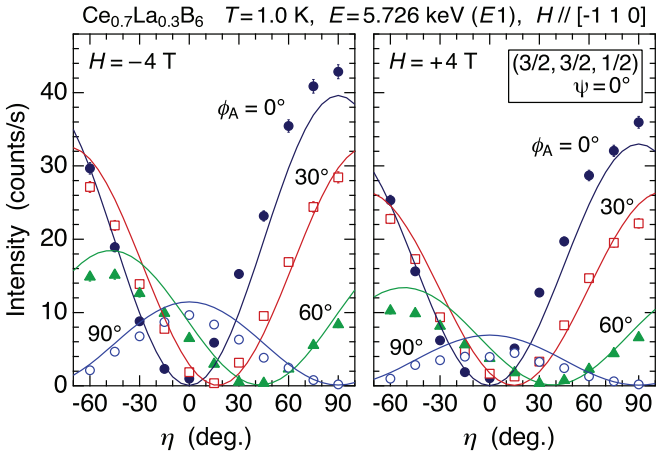

FIG. 15. (Color online) Incident polarization dependencies of the $E1$ intensity at $H = \pm 4$ T. Solid lines are the calculations.

Let us finally analyze the result of the $E2$ resonance in Fig. 16. As in the L_2 edge, we need to consider the interference between the $E1$ and $E2$ resonances. The full expression of the scattering amplitude operator is given by Eq. (6), where we use the spectral functions for the L_3 edge. Although Eq. (6) contains all the contributions from rank-1 to rank-3, in the present analysis of the $E2$ resonance at the L_3 edge, by contrast, we can neglect the rank-1 contribution as shown in the previous study on CeB_6. Therefore the model scattering amplitude at $H = \pm 4$ T and $\hbar\omega = 5.719$ keV (L_3-$E2$) is written as

$$\begin{aligned}\hat{F}_{\pm} = &\pm |\alpha_{E1}^{(2)}| e^{i\delta_1^{(2)}} \left(\hat{G}_{E1}^{O_{yz}} - \hat{G}_{E1}^{O_{zx}}\right)\langle O_{yz}\rangle \\ &\pm |\alpha_{E2}^{(2)}| e^{i\delta_2^{(2)}} \left(\hat{G}_{E2}^{O_{yz}} - \hat{G}_{E1}^{O_{zx}}\right)\langle O_{yz}\rangle \\ &+ |\alpha_{E2}^{(3)}| e^{i\delta_2^{(3)}} \left(\hat{G}_{E2}^{T_z^\alpha}\langle T_z^\alpha\rangle + \hat{G}_{E2}^{T_{xyz}}\langle T_{xyz}\rangle\right). \qquad (7)\end{aligned}$$

In this case, the situation is better than the case in the L_2 edge where the reliable determination of the parameter was unsuccessful. Nevertheless, it is still not possible to determine the parameters uniquely. There is a range of values in which any set of parameters can reproduce the data in the same manner, which is summarized in Table IV. The solid lines in Fig. 16 are the calculations using a parameter set: $|\alpha_{E1}^{(2)}|\langle O_{yz}\rangle = 3.4$, $|\alpha_{E2}^{(2)}|\langle O_{yz}\rangle = 1.2$, $|\alpha_{E2}^{(3)}|\langle T_z^\alpha\rangle = 6$, $|\alpha_{E2}^{(3)}|\langle T_{xyz}\rangle = 10$, $\delta_1^{(2)} - \delta_2^{(3)} = 0.08$, and $\delta_2^{(2)} - \delta_2^{(3)} = -0.28$. These values are in the middle of the range in Table IV. We note that, in the previous report of Ref. [29] on CeB_6, relative ratios among various multipoles as shown in Table IV have not been discussed. We are dealing with the same ordered state in more detail.

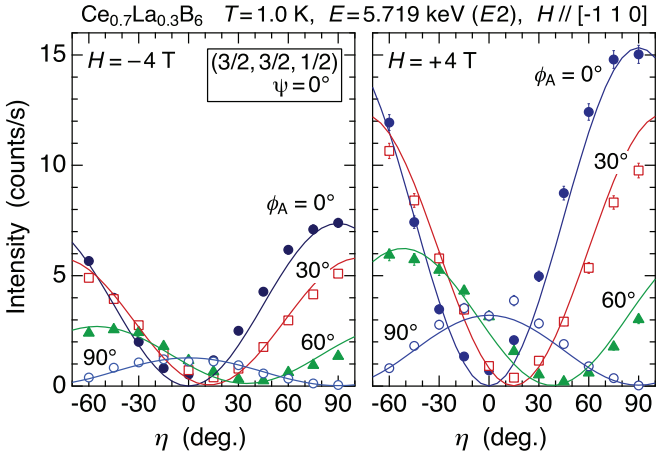

FIG. 16. (Color online) Incident polarization dependencies of the $E2$ intensity at $H = \pm 4$ T. Solid lines are the calculations.

TABLE IV. The parameters in Eq. (7) to explain the result of Fig. 16.

$\lvert\alpha_{E1}^{(2)}\rvert \cdot \langle O_{yz}\rangle$	$\lvert\alpha_{E2}^{(2)}\rvert \cdot \langle O_{yz}\rangle$	$\lvert\alpha_{E2}^{(3)}\rvert \cdot \langle T_z^\alpha\rangle$	$\lvert\alpha_{E2}^{(3)}\rvert \cdot \langle T_{xyz}\rangle$	$\delta_1^{(2)} - \delta_2^{(3)}$	$\delta_2^{(2)} - \delta_2^{(3)}$
3.7	1.34	4.6	8	0.1	−0.2
⋮	⋮	⋮	⋮	⋮	⋮
2.8	1.07	7.9	13	0.05	−0.4

To understand the interference effect more explicitly, let us examine which parameter determines the total intensity. By taking all the multipoles into account, we obtain $I_{\pi\sigma'}(+4\text{ T}) = 14.8$, $I_{\pi\sigma'}(-4\text{ T}) = 7.3$, $I_{\sigma\pi'}(+4\text{ T}) = 3.1$, and $I_{\sigma\pi'}(-4\text{ T}) = 1.2$, which well reproduce the data in Fig. 16. If we take into account only $|\alpha_{E1}^{(2)}|\langle O_{yz}\rangle$ and $|\alpha_{E2}^{(3)}|\langle T_{xyz}\rangle$, we obtain $I_{\pi\sigma'}(+4\text{ T}) = 13.1$ and $I_{\pi\sigma'}(-4\text{ T}) = 8.9$, which nearly explains the data for π-σ'. Thus most of the π-σ' intensity is determined by these two terms. This is how the resonant intensity for π-σ' was analyzed in CeB_6 previously [29]. However, for σ-π', with these parameters only, we have $I_{\sigma\pi'}(+4\text{ T}) = 11.7$ and $I_{\sigma\pi'}(-4\text{ T}) = 8.8$, which is far from agreement with the data. This disagreement is removed by including $|\alpha_{E2}^{(3)}|\langle T_z^\alpha\rangle$: we have $I_{\pi\sigma'}(+4\text{ T}) = 13.2$, $I_{\pi\sigma'}(-4\text{ T}) = 9.0$, $I_{\sigma\pi'}(+4\text{ T}) = 2.4$, and $I_{\sigma\pi'}(-4\text{ T}) = 1.7$. While the π-σ' intensities are not affected, the agreement in the σ-π' intensity is significantly improved. The $|\alpha_{E2}^{(2)}|\langle O_{yz}\rangle$ term slightly modifies the final intensity to improve the total agreement.

The fitting result of Table IV shows that $|\alpha_{E2}^{(3)}|\langle T_{xyz}\rangle$ at 4 T is more than 8 at least. From Fig. 10 of Ref. [29], $\langle T_{xyz}\rangle$ at 4 T is estimated to be induced almost to the full moment. Therefore, let us consider $|\alpha_{E2}^{(3)}|\langle T_{xyz}\rangle = 8$, which gives the intensity in cps unit, as the value corresponding to the full moment of $\langle T_{xyz}\rangle$. The theoretical value of the $\langle T_{xyz}\rangle$ full moment is $9\sqrt{5}/2 = 10.06$ in the Γ_8 CEF ground state. In the same manner, the theoretical full moment of $\langle T^\beta\rangle \equiv \langle T_x^\beta + T_y^\beta + T_z^\beta\rangle/3$, the order parameter of phase IV at $H = 0$ T where $\langle T_x^\beta\rangle = \langle T_y^\beta\rangle = \langle T_z^\beta\rangle$ is satisfied, is $\sqrt{30} = 5.48$.

Next, let us estimate the intensity at $H = 0$ T in the $\langle T^\beta\rangle$-AFO phase, which was too weak to be detected. The scattering amplitude operator for domains 1 and 2 at $H = 0$ T and $\hbar\omega = 5.719$ keV (L_3-$E2$) is written as

$$\hat{F}_1 = |\alpha_{E2}^{(3)}| e^{i\delta_2^{(3)}} \left(\hat{G}_{E2}^{T_x^\beta} + \hat{G}_{E2}^{T_y^\beta} + \hat{G}_{E2}^{T_z^\beta}\right)\langle T^\beta\rangle, \qquad (8a)$$

$$\hat{F}_2 = |\alpha_{E2}^{(3)}| e^{i\delta_2^{(3)}} \left(\hat{G}_{E2}^{T_x^\beta} - \hat{G}_{E2}^{T_y^\beta} + \hat{G}_{E2}^{T_z^\beta}\right)\langle T^\beta\rangle. \qquad (8b)$$

Experimentally, from Fig. 8, the σ-σ' and π-σ' intensity at 0 T is estimated to be less than 0.2 and 0.1 cps, respectively. If we put $|\alpha^{(3)}_{E2}|\langle T^\beta\rangle = (8 \times 5.48/10.06)/4$, corresponding to one-fourth of the full moment value, we have $I_{\sigma\sigma'} = 0.22$ cps and $I_{\pi\sigma'} = 0.066$ cps, and these are the largest values we can expect as the hidden signals from the $\langle T^\beta\rangle$-AFO order for the $E2$ intensity at the L_3 edge. Thus we conclude that the $\langle T^\beta\rangle$-AFO order parameter at $T = 1.0$ K is less than one-fourth of the full moment.

Finally, let us go back to the T dependence of the σ-σ' intensity at the L_2 edge shown in Fig. 3. From the observed intensity of $\sim$1 cps at 1.0 K, it is estimated that the full moment of the $\langle T^\beta\rangle$-AFO order would give an intensity larger than $1 \times 4^2 = 16$ cps because the intensity is proportional to the square of the order parameter. In actuality, from Fig. 3, the intensity increases with decreasing temperature and is expected to saturate at around 2.5 cps at $T = 0$ K. Therefore the value of the T^β-AFO at $T = 0$ K is estimated to be less than $\sqrt{2.5/16} = 0.4$ times the full moment.

IV. DISCUSSION

The experiment shows that both the Γ_{3g}- and Γ_{5g}-AFQ are induced by the field in the Γ_{5u}-AFO phase as expected in Table I. Remarkably, however, the Γ_{5g}-AFQ is induced more than the Γ_{3g}-AFQ as shown by the L_2- and L_3-edge experiments. This is an important problem because it is contradictory to what is expected from an MF calculation for the Γ_{5u}-AFO order, which is shown in Fig. 17 and described in the following.

We consider the following Hamiltonian for the MF calculation:

$$\mathcal{H} = \sum_i [\mathcal{H}_{\rm CEF} - g\mu_{\rm B}\boldsymbol{J}(i)\cdot\boldsymbol{H}] - \sum_{i,j} K^{(\rm o)}_{5u}\boldsymbol{T}^\beta(i)\cdot\boldsymbol{T}^\beta(j) - \sum_{i,j} K^{(\rm q)}_{5g}\boldsymbol{O}_{\Gamma_{5g}}(i)\cdot\boldsymbol{O}_{\Gamma_{5g}}(j) - \sum_{i,j} K^{(\rm o)}_{2u}T_{xyz}(i)T_{xyz}(j), \quad (9)$$

where $\mathcal{H}_{\rm CEF}$ is the cubic CEF giving the Γ_8 ground state. The Γ_{5g} quadrupole, Γ_{5u} octupole, and Γ_{2u} octupole exchange interactions are represented by $K^{(\rm q)}_{5g}$, $K^{(\rm o)}_{5u}$, and $K^{(\rm o)}_{2u}$, respectively. We treat the Hamiltonian in a two-sublattice model. If we consider $K^{(\rm q)}_{5g}$=−0.6 K only, we have an Γ_{5g}-AFQ transition temperature of 0.6 K at $H = 0$ T, which is represented by $T^{(q)}_{5g} = 0.6$ K in Fig. 17. In the same manner, the AFO parameters $K^{(\rm o)}_{5u}$ and $K^{(\rm o)}_{2u}$ are transformed to the respective transition temperatures, $T^{(o)}_{5u}$ and $T^{(o)}_{2u}$, at zero field. In all cases, the primary order parameter is the $\Gamma_{5u}(T^\beta)$-AFO as shown in Fig. 17(d) and accompanies the Γ_{5g}-type ferroquadrupole order as shown in Fig. 17(e).

The calculated H dependencies of the order parameters we treated in Sec. III are shown in Figs. 17(a)–17(c). As we assumed in Sec. III, the even and odd rank multipoles are induced linearly and quadratically with H, respectively, and the sign does and does not change with the field reversal. It is noted that the $\Gamma_{4u}(T^\alpha)$-AFO is induced in the same manner as the AFM dipole moment since they belong to the same irreducible representation.

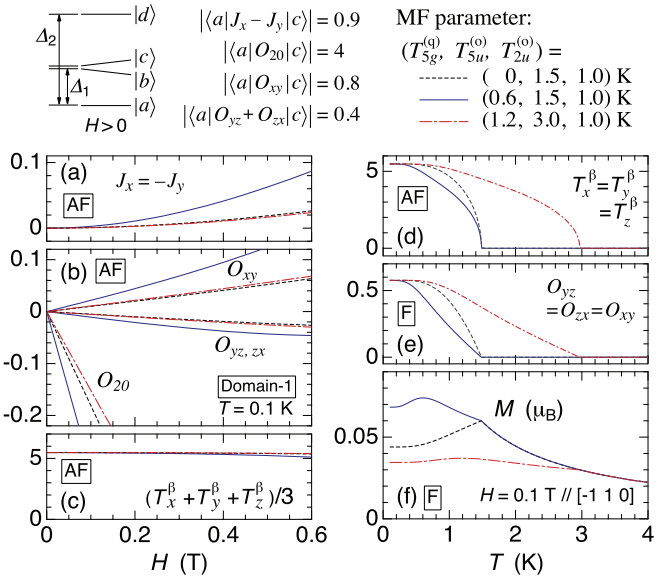

FIG. 17. (Color online) Results of the MF calculation of Eq. (9). The interaction parameters are represented by the respective transition temperatures: $K^{(\rm q)}_{5g}$, $T^{(o)}_{5u}$, and $T^{(o)}_{2u}$. (a)–(c) H dependencies of the AFM dipole, AFQ, and Γ_{5u}-AFO moments, respectively, for domain 1 at $T = 0.1$ K. (d) and (e) T dependencies of the Γ_{5u}-AFO and Γ_{5g}-FQ moments, respectively, at $H = 0$ T. (f) T dependencies of the domain averaged uniform magnetization. The primary $\Gamma_{5u}(T^\beta)$-AFO is realized at zero field in all cases. Energy-level splitting of the Γ_8 CEF ground state and the off-diagonal matrix elements responsible for the field-induced dipole and quadrupole moments are also shown.

The most significant discrepancy between the MF calculation and the experimental result is that the Γ_{3g}-AFQ in the MF model is much more ($\sim$10 times) strongly induced than the Γ_{5g}-AFQ because of the large off-diagonal matrix element as shown in Fig. 17. Although the parameters for the Γ_{3g}- and Γ_{5g}-AFQ moments in Tables II and III were chosen so that their signs and ratios were as consistent as possible with the MF calculation, they are still far from those in Fig. 17(b). The cusp anomaly in $M(T)$ reported in Ref. [20] is also difficult to explain by an MF model if we take into account the Γ_{5g}-AFQ interaction as shown by the solid line in Fig. 17(f) [33]. Although the cusp anomaly is reproduced without the AFQ interaction as shown by the dashed line, the anomaly disappears if we consider the AFQ interaction as shown by the solid line. Since the AFQ interaction should exist in this system behind the octupole order, the MF model has a severe difficulty in explaining the experimental results.

We consider that these difficulties are the consequence of multipolar fluctuation. The AFQ transition temperature of CeB_6 in the MF model is estimated to be $\sim$7 K at zero field, which is twice as large as the actual value of 3.3 K [45]. In Fig. 1, we notice that the curvature of the phase line at low fields, reflecting the multipolar fluctuation effect, is more significant in $Ce_{0.7}La_{0.3}B_6$ than in CeB_6. It is suggested that the AFQ, AFO, and AFM order parameters are in strong competition. Therefore the actual AFO transition at 1.5 K is supposed to be a consequence of strong fluctuation. The AFO transition temperature in the MF model can possibly be as high as 3 K, which would reduce the magnetization at the lowest

temperature to a value represented by the single dotted line in Fig. 17(f). This would make a cusp if the actual transition temperature is reduced to 1.5 K due to fluctuation. The resonant $E1$ signal remaining above the transition temperature reported in Ref. [8] might be associated with the fluctuation, which is an unresolved problem and requires further study. A direct observation of the excitation energy (Δ_1 and Δ_2 in Fig. 17) in the Γ_{5u}-AFO phase by inelastic neutron scattering will also be important in clarifying the intrinsic strength of the AFO interaction.

It should also be noted that the phases of Γ_{5u}-AFO and the Γ_{5g}-AFQ (with Γ_{4u}-AFM inside) are separated by a first-order transition due to incompatible symmetries. In this transition, the strongly induced Γ_{5g}-AFQ below 1 T is also considered to reflect an underlying fluctuation, which is associated with an instability to the AFQ order in the AFO phase; it cannot be explained by changing the MF parameters as shown in Fig. 17(b). Furthermore, since the induction of the Γ_{5g}-AFQ occurs at low temperatures in the ordered phase where the thermal fluctuation is suppressed and the MF behavior is expected, quantum fluctuation is supposed to play an essential role.

Another experimental fact that is supposed to be associated with the quantum fluctuation is the reduction of the ordered magnetic dipole moment ($0.3 \sim 0.4\ \mu_B$) in the AFM phase of $Ce_xLa_{1-x}B_6$ [46–48]. It is not probable to ascribe this to the Kondo effect alone, since the uniform magnetization soon reaches 1 μ_B in magnetic fields and is explained by the MF calculation [49]. It is speculated that the close degeneracy among the AFM, AFQ, and AFO orderings causes the quantum fluctuation and results in the reduction of the ordered moments. In the present study, we showed that the Γ_{5u}-AFO moment is reduced from its full moment value, although the estimation process was rather indirect. An abrupt appearance of the AFM dipole order by a magnetic ion doping into the AFO phase also seems to suggest the underlying instability to the AFM dipole order [33]. The characteristic phase boundary we pointed out in Sec. I may be related with these nearly degenerate ordered phases of AFO, AFQ, and AFM, which are symmetrically incompatible with each other. In any case, further experimental study is necessary and deserves to be performed from the viewpoint of fluctuation.

V. CONCLUSION

By utilizing resonant x-ray diffraction in magnetic fields with full linear polarization analysis, we have identified the field-induced multipole order parameters of $Ce_{0.7}La_{0.3}B_6$, and thereby extracted a hidden AFQ fluctuation in the Γ_{5u}-AFO ordered phase. Although the Γ_{5u}-AFO should favor the Γ_{3g}-AFQ as the main induced moment, the Γ_{5g}-AFQ was actually induced much more than the Γ_{3g}-AFQ. This is considered to be caused by strong multipolar fluctuation associated with the competition among active multipole order parameters. We also remark that investigation of the field-induced staggered multipoles on the primary AF-order by RXD thus provides valuable information on the hidden multipolar interactions, which strongly affect the ordering phenomenon but cannot be revealed only by studying the primary order parameter.

ACKNOWLEDGMENTS

The authors thank R. Shiina for valuable discussions. This work was supported by Grants-in-Aid for Scientific Research (Nos. 21204456 and 24340087) from the Japan Society for the Promotion of Science (JSPS), by a Grant-in-Aid for Scientific Research on Innovative Areas "Heavy Electrons" (No. 21102515) from the Ministry of Education, Culture, Sports, Science, and Technology (MEXT), and by a Basic Science Research Grant from the Sumitomo Foundation. The synchrotron radiation experiments were performed under Proposal Nos. 2010B3711, 2011A3711, and 2011B3711 at BL22XU of SPring-8.

APPENDIX A: FORMALISM OF POLARIZATION ANALYSIS

We use the scattering-amplitude-operator method to analyze the results of full-linear-polarization-analysis measurements [44]. This method is useful for describing the observed intensity at the detector in a general scattering geometry shown in Fig. 2, where the incident polarization angle is rotated by the phase plates and a crystal analyzer system is inserted to analyze the polarization state of the scattered x ray.

We consider a 2×2 matrix $\hat{F}$ consisting of four elements of the scattering amplitude for σ-σ', σ-π', π-σ', and π-π' processes:

$$\hat{F} = \begin{pmatrix} F_{\sigma\sigma'} & F_{\pi\sigma'} \\ F_{\sigma\pi'} & F_{\pi\pi'} \end{pmatrix}. \tag{A1}$$

This determines the state of the target system. By using the identity matrix $\hat{I}$ and the Pauli matrix $\hat{\boldsymbol{\sigma}}$, $\hat{F}$ can generally be expressed as

$$\hat{F} = \beta\hat{I} + \boldsymbol{\alpha}\cdot\hat{\boldsymbol{\sigma}} = \begin{pmatrix} \beta+\alpha_3 & \alpha_1 - i\alpha_2 \\ \alpha_1 + i\alpha_2 & \beta - \alpha_3 \end{pmatrix}, \tag{A2}$$

where the parameters β and $\boldsymbol{\alpha} = (\alpha_1,\alpha_2,\alpha_3)$ are

$$\begin{aligned} \beta &= (F_{\sigma\sigma'} + F_{\pi\pi'})/2, \quad \alpha_1 = (F_{\pi\sigma'} + F_{\sigma\pi'})/2, \\ \alpha_2 &= i(F_{\pi\sigma'} - F_{\sigma\pi'})/2, \quad \alpha_3 = (F_{\sigma\sigma'} - F_{\pi\pi'})/2. \end{aligned} \tag{A3}$$

Next, to calculate the scattering cross-section, information on the incident photon state is necessary. This is described by the density matrix $\hat{\mu} = (\hat{I} + \boldsymbol{P}\cdot\hat{\boldsymbol{\sigma}})/2$, where the Stokes vector $\boldsymbol{P} = (P_1, P_2, P_3)$ represents the polarization state of the incident photon. P_1, P_2, and P_3 represent $\pm 45^\circ$, left- or right-handed circular, and σ or π polarization state, respectively [44]. For example, $\boldsymbol{P} = (0,0,1)$ and $(0,0,-1)$ mean the perfectly σ and π polarized state, i.e., $\eta = 0^\circ$ and 90° in Fig. 2, respectively. In general, since the beam is not perfectly polarized, we need to consider a situation with ${P_1}^2 + {P_2}^2 + {P_3}^2 < 1$.

Once we know the matrix $\hat{F}$, the scattering cross-section $(d\sigma/d\Omega)$ can be calculated by

$$\begin{aligned} \left(\frac{d\sigma}{d\Omega}\right) = \mathrm{Tr}(\hat{\mu}\hat{F}^\dagger\hat{F}) &= \beta^\dagger\beta + \boldsymbol{\alpha}^\dagger\cdot\boldsymbol{\alpha} + \beta^\dagger(\boldsymbol{P}\cdot\boldsymbol{\alpha}) \\ &\quad + (\boldsymbol{P}\cdot\boldsymbol{\alpha}^\dagger)\beta + i\,\boldsymbol{P}\cdot(\boldsymbol{\alpha}^\dagger\times\boldsymbol{\alpha}). \end{aligned} \tag{A4}$$

The Stokes vector of the scattered x ray, $\boldsymbol{P}'$, can be obtained from

$$\left(\frac{d\sigma}{d\Omega}\right)\boldsymbol{P}' = \mathrm{Tr}(\hat{\mu}\hat{F}^{\dagger}\hat{\boldsymbol{\sigma}}\hat{F}) = \beta^{\dagger}\boldsymbol{\alpha} + \boldsymbol{\alpha}^{\dagger}\beta - i(\boldsymbol{\alpha}^{\dagger}\times\boldsymbol{\alpha}) + \beta^{\dagger}\beta\boldsymbol{P} - i\beta^{\dagger}(\boldsymbol{P}\times\boldsymbol{\alpha}) + i(\boldsymbol{P}\times\boldsymbol{\alpha}^{\dagger})\beta + \boldsymbol{\alpha}^{\dagger}(\boldsymbol{P}\cdot\boldsymbol{\alpha}) - \boldsymbol{\alpha}^{\dagger}\times(\boldsymbol{P}\times\boldsymbol{\alpha}). \quad \text{(A5)}$$

As an example, we show a case of fundamental Bragg reflection from the crystal lattice by nonresonant Thomson scattering. In this case, the scattering amplitude is written as

$$\hat{F} = -F_c\begin{pmatrix}1 & 0\\ 0 & \cos 2\theta\end{pmatrix}, \quad \text{(A6)}$$

where F_c represents the structure factor of the reflection. From Eq. (A3), $\beta = -F_c\cos^2\theta$, $\alpha_1 = \alpha_2 = 0$, and $\alpha_3 = -F_c\sin^2\theta$ are obtained. Then, from Eq. (A4), the scattering cross-section becomes

$$\left(\frac{d\sigma}{d\Omega}\right) = |F_c|^2\left[1 - \frac{1}{2}(1-P_3)\sin^2 2\theta\right], \quad \text{(A7)}$$

and from Eq. (A5), $\boldsymbol{P}'$ satisfies

$$\left(\frac{d\sigma}{d\Omega}\right)P_1' = |F_c|^2 P_1\cos 2\theta\ ,$$
$$\left(\frac{d\sigma}{d\Omega}\right)P_2' = |F_c|^2 P_2\cos 2\theta\ , \quad \text{(A8)}$$
$$\left(\frac{d\sigma}{d\Omega}\right)P_3' = |F_c|^2\left[P_3 + \frac{1}{2}(1-P_3)\sin^2 2\theta\right].$$

The Stokes vector of the incident x ray, with the polarization angle η in Fig. 2, is written as

$$\boldsymbol{P} = P_L(\sin 2\eta,\ 0,\ \cos 2\eta), \quad \text{(A9)}$$

where P_L represents the degree of linear polarization. In the present experiment at $E = 6.160$ keV, for example, P_L is 0.978 at $\eta = 0^\circ$ and over 0.999 at $\eta = 90^\circ$, and can be written as $P_L = 0.999 - 0.022\cos^2\eta$ [37].

The intensity after diffracted by the analyzer crystal is also described by the Thomson scattering, and Eq. (A7) is applied. It is noted, however, that P_3 must be transformed to the value for the diffraction at the analyzer, which we write as P_{3A}:

$$P_{3\mathrm{A}} = P_1'\sin 2\phi_{\mathrm{A}} + P_3'\cos 2\phi_{\mathrm{A}}. \quad \text{(A10)}$$

Finally, the intensity at the detector is expressed as

$$I = K\left(\frac{d\sigma}{d\Omega}\right)\left[1 - \frac{1}{2}(1-P_{3\mathrm{A}})\sin^2 2\theta_{\mathrm{A}}\right], \quad \text{(A11)}$$

where $(d\sigma/d\Omega)$ is the scattering cross-section of the sample expressed by Eq. (A7) and K represents a constant factor.

In Fig. 18, we show the experimental result of polarization analysis for the 111 fundamental Bragg reflection. The solid lines are the calculated curves with Eq. (A11), which explains the data very well and supports the reliability of the data described in the main text.

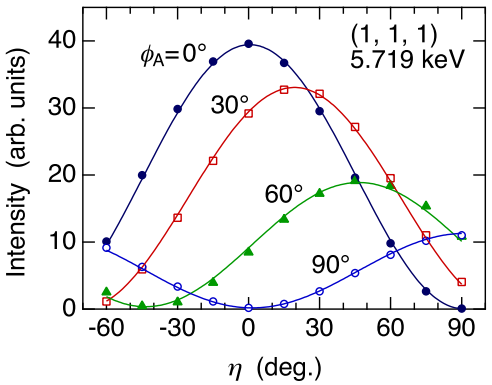

FIG. 18. (Color online) Incident polarization dependencies of the 111 fundamental Bragg reflection by nonresonant Thomson scattering. Solid lines are the calculations with Eq. (A11).

APPENDIX B: RESONANT SCATTERING AMPLITUDE

Let us briefly summarize the theoretical framework of resonant x-ray diffraction given by Nagao and Igarashi in Ref. [28]. The scattering cross-section at an x-ray energy $E = \hbar\omega$ is proportional to $|F_{E1}(\omega) + F_{E2}(\omega)|^2$, where F_{E1} and F_{E2} are the resonant scattering amplitudes for the $E1$ and $E2$ processes, respectively. They are expressed as

$$F_{E1}(\omega) = \sum_{\nu=0}^{2}\alpha_{E1}^{(\nu)}(\omega)\sum_{\mu=1}^{2\nu+1}G_{E1,\mu}^{(\nu)}(\boldsymbol{\varepsilon},\boldsymbol{\varepsilon}')\langle z_\mu^{(\nu)}\rangle, \quad \text{(B1)}$$

$$F_{E2}(\omega) = \sum_{\nu=0}^{4}\alpha_{E2}^{(\nu)}(\omega)\sum_{\mu=1}^{2\nu+1}G_{E2,\mu}^{(\nu)}(\boldsymbol{\varepsilon},\boldsymbol{\varepsilon}',\hat{\boldsymbol{k}},\hat{\boldsymbol{k}}')\langle z_\mu^{(\nu)}\rangle. \quad \text{(B2)}$$

$z_\mu^{(\nu)}$ represents the μth component of the rank-ν multipole tensor, which are defined in Table I of Ref. [39]. In the data analysis, the expectation value $\langle z_\mu^{(\nu)}\rangle$ is regarded as an order parameter. Conventional notations of multipoles such as T_x^α also follows the table. The multipolar order parameters appearing in the present paper is summarized in Table V. $G_{E1,\mu}^{(\nu)}$ and $G_{E2,\mu}^{(\nu)}$ are the geometrical factors for the $E1$ and

TABLE V. Multipolar order parameters in the Γ_8-quartet ground state as classified by the rank and the irreducible representation (Irrep).

ν	Irrep	$z_\mu^{(\nu)}$
1	Γ_{4u}	J_x, J_y, J_z
2	Γ_{3g}	O_{20}, O_{22}
2	Γ_{5g}	O_{yz}, O_{zx}, O_{xy}
3	Γ_{2u}	T_{xyz}
3	Γ_{4u}	$T_x^\alpha, T_y^\alpha, T_x^\alpha$
3	Γ_{5u}	$T_x^\beta, T_y^\beta, T_x^\beta$

$E2$ resonances by $\langle z_\mu^{(\nu)}\rangle$, respectively, which are fully written in Refs. [28] and [39]. The most important point in these expressions is that the rank dependent energy profiles, $\alpha_{E1}^{(\nu)}(\omega)$ and $\alpha_{E2}^{(\nu)}(\omega)$, are used. This point plays an important role in the interference effect between $E1$ and $E2$ resonances and also between resonances by multipoles of different ranks.

Given the scattering geometry, we can calculate $G_{E1,\mu}^{(\nu)}(\boldsymbol{\varepsilon},\boldsymbol{\varepsilon}')$ and $G_{E2,\mu}^{(\nu)}(\boldsymbol{\varepsilon},\boldsymbol{\varepsilon}',\hat{\boldsymbol{k}},\hat{\boldsymbol{k}}')$ for σ-σ', σ-π', π-σ', and π-π' processes. Then, we obtain 2×2 matrices $\hat{G}_{E1,\mu}$ and $\hat{G}_{E2,\mu}$, and the scattering amplitude matrices for $E1$ and $E2$ resonances are written as

$$\hat{F}_{E1}(\omega)=\sum_{\nu=0}^{2}\alpha_{E1}^{(\nu)}(\omega)\sum_{\mu=1}^{2\nu+1}\hat{G}_{E1,\mu}^{(\nu)}\langle z_\mu^{(\nu)}\rangle, \tag{B3}$$

$$\hat{F}_{E2}(\omega)=\sum_{\nu=0}^{4}\alpha_{E2}^{(\nu)}(\omega)\sum_{\mu=1}^{2\nu+1}\hat{G}_{E2,\mu}^{(\nu)}\langle z_\mu^{(\nu)}\rangle. \tag{B4}$$

The followings are the $\hat{G}$ matrices for $\boldsymbol{k}-\boldsymbol{k}'=(\frac{3}{2},\frac{3}{2},\frac{1}{2})$ in CeB_6 at $\psi=0^\circ$ at the L_2 edge ($E=6.160$ keV for $E2$ and $E=6.168$ keV for $E1$). At the L_3 edge, although we do not list them, the values are approximately 5% to 10% different from those of the L_2 edge due to the difference in the Bragg angle θ.

$$\hat{G}_{E1}^{J_x}=i\begin{pmatrix}0.0000 & 0.5017\\ 0.2264 & -0.6348\end{pmatrix},\quad \hat{G}_{E1}^{J_y}=i\begin{pmatrix}0.0000 & 0.5017\\ 0.2264 & 0.6348\end{pmatrix},\quad \hat{G}_{E1}^{J_z}=i\begin{pmatrix}0.0000 & -0.7047\\ 0.9474 & 0.0000\end{pmatrix},$$
$$\hat{G}_{E1}^{O_{20}}=\begin{pmatrix}-0.5000 & 0.0000\\ 0.0000 & -0.5609\end{pmatrix},\quad \hat{G}_{E1}^{O_{22}}=\begin{pmatrix}0.0000 & 0.6103\\ 0.8204 & 0.0000\end{pmatrix},$$
$$\hat{G}_{E1}^{O_{yz}}=\begin{pmatrix}0.0000 & -0.4345\\ 0.1961 & 0.2735\end{pmatrix},\quad \hat{G}_{E1}^{O_{zx}}=\begin{pmatrix}0.0000 & 0.4345\\ -0.1961 & 0.2735\end{pmatrix},\quad \hat{G}_{E1}^{O_{xy}}=\begin{pmatrix}-0.8660 & 0.0000\\ 0.0000 & 0.5781\end{pmatrix}, \tag{B5}$$

$$\hat{G}_{E2}^{J_x}=i\begin{pmatrix}-0.1507 & 0.1584\\ 0.1663 & -0.2647\end{pmatrix},\quad \hat{G}_{E2}^{J_y}=i\begin{pmatrix}0.1507 & 0.1584\\ 0.1663 & 0.2647\end{pmatrix},\quad \hat{G}_{E2}^{J_z}=i\begin{pmatrix}0.0000 & 0.0780\\ 0.0303 & 0.0000\end{pmatrix},$$
$$\hat{G}_{E2}^{O_{20}}=\begin{pmatrix}-0.2250 & 0.0000\\ 0.0000 & 0.1231\end{pmatrix},\quad \hat{G}_{E2}^{O_{22}}=\begin{pmatrix}0.0000 & 0.1141\\ -0.0443 & 0.0000\end{pmatrix},\quad \hat{G}_{E2}^{O_{yz}}=\begin{pmatrix}0.1096 & 0.2319\\ -0.2435 & 0.0000\end{pmatrix},$$
$$\hat{G}_{E2}^{O_{zx}}=\begin{pmatrix}0.1096 & -0.2319\\ 0.2435 & 0.0000\end{pmatrix},\quad \hat{G}_{E2}^{O_{xy}}=\begin{pmatrix}0.2316 & 0.0000\\ 0.0000 & 0.2133\end{pmatrix},\quad \hat{G}_{E2}^{T_{xyz}}=i\begin{pmatrix}0.0000 & -0.1473\\ 0.1982 & 0.0000\end{pmatrix}, \tag{B6}$$
$$\hat{G}_{E2}^{T_x^\alpha}=i\begin{pmatrix}-0.0753 & 0.2777\\ 0.1729 & 0.0331\end{pmatrix},\quad \hat{G}_{E2}^{T_y^\alpha}=i\begin{pmatrix}0.0753 & 0.2777\\ 0.1729 & -0.0331\end{pmatrix},\quad \hat{G}_{E2}^{T_z^\alpha}=i\begin{pmatrix}0.0000 & 0.0343\\ -0.3164 & 0.0000\end{pmatrix},$$
$$\hat{G}_{E2}^{T_x^\beta}=i\begin{pmatrix}0.2918 & 0.1547\\ -0.1136 & -0.1281\end{pmatrix},\quad \hat{G}_{E2}^{T_y^\beta}=i\begin{pmatrix}0.2918 & -0.1547\\ 0.1136 & -0.1281\end{pmatrix},\quad \hat{G}_{E2}^{T_z^\beta}=i\begin{pmatrix}0.0000 & 0.0000\\ 0.0000 & 0.0000\end{pmatrix}.$$

[1] P. Santini, S. Carretta, G. Amoretti, R. Caciuffo, N. Magnani, and G. H. Lander, Rev. Mod. Phys. **81**, 807 (2009).

[2] Y. Kuramoto, H. Kusunose, and A. Kiss, J. Phys. Soc. Jpn. **78**, 072001 (2009).

[3] J. M. Effantin, J. Rossat-Mignod, P. Burlet, H. Bartholin, S. Kunii, and T. Kasuya, J. Magn. Magn. Mater. **47-48**, 145 (1985).

[4] T. Onimaru, T. Sakakibara, N. Aso, H. Yoshizawa, H. S. Suzuki, and T. Takeuchi, Phys. Rev. Lett. **94**, 197201 (2005).

[5] T. Matsumura, N. Oumi, K. Hirota, H. Nakao, Y. Murakami, Y. Wakabayashi, T. Arima, S. Ishihara, and Y. Endoh, Phys. Rev. B **65**, 094420 (2002).

[6] P. Link, A. Gukasov, J.-M. Mignot, T. Matsumura, and T. Suzuki, Phys. Rev. Lett. **80**, 4779 (1998).

[7] H. C. Walker, K. A. McEwen, D. F. McMorrow, S. B. Wilkins, F. Wastin, E. Colineau, and D. Fort, Phys. Rev. Lett. **97**, 137203 (2006).

[8] D. Mannix, Y. Tanaka, D. Carbone, N. Bernhoeft, and S. Kunii, Phys. Rev. Lett. **95**, 117206 (2005).

[9] H. Kusunose and Y. Kuramoto, J. Phys. Soc. Jpn. **74**, 3139 (2005).

[10] K. Kuwahara, K. Iwasa, M. Kohgi, N. Aso, M. Sera, and F. Iga, J. Phys. Soc. Jpn. **76**, 093702 (2007).

[11] P. Santini, S. Carretta, N. Magnani, G. Amoretti, and R. Caciuffo, Phys. Rev. Lett. **97**, 207203 (2006).

[12] N. Magnani, S. Carretta, R. Caciuffo, P. Santini, G. Amoretti, A. Hiess, J. Rebizant, and G. H. Lander, Phys. Rev. B **78**, 104425 (2008).

[13] G. Friemel, Y. Li, A. V. Dukhnenko, N. Y. Shitsevalova, N. E. Sluchanko, A. Ivanov, V. B. Filipov, B. Keimer, and D. S. Inosov, Nat. Commun. **3**, 830 (2012).

[14] A. Akbari and P. Thalmeier, Phys. Rev. Lett. **108**, 146403 (2012).

[15] R. Shiina, H. Shiba, and P. Thalmeier, J. Phys. Soc. Jpn. **66**, 1741 (1997).

[16] H. Shiba, O. Sakai, and R. Shiina, J. Phys. Soc. Jpn. **68**, 1988 (1999).

[17] H. Kusunose and Y. Kuramoto, J. Phys. Soc. Jpn. **70**, 1751 (2001).

[18] S. Carretta, P. Santini, R. Caciuffo, and G. Amoretti, Phys. Rev. Lett. **105**, 167201 (2010).
[19] R. Caciuffo, P. Santini, S. Carretta, G. Amoretti, A. Hiess, N. Magnani, L.-P. Regnault, and G. H. Lander, Phys. Rev. B **84**, 104409 (2011).
[20] T. Tayama, T. Sakakibara, K. Tenya, H. Amitsuka, and S. Kunii, J. Phys. Soc. Jpn. **66**, 2268 (1997).
[21] O. Suzuki, T. Goto, S. Nakamura, T. Matsumura, and S. Kunii, J. Phys. Soc. Jpn. **67**, 4243 (1998).
[22] S. Kobayashi, M. Sera, M. Hiroi, N. Kobayashi, and S. Kunii, J. Phys. Soc. Jpn. **69**, 926 (2000).
[23] M. Akatsu, T. Goto, Y. Nemoto, O. Suzuki, S. Nakamura, and S. Kunii, J. Phys. Soc. Jpn. **72**, 205 (2003).
[24] M. Akatsu, T. Goto, O. Suzuki, Y. Nemoto, S. Nakamura, S. Kunii, and G. Kido, Phys. Rev. Lett. **93**, 156409 (2004).
[25] R. G. Goodrich, D. P. Young, D. Hall, L. Balicas, Z. Fisk, N. Harrison, J. B. Betts, A. Migliori, F. M. Woodward, and J. W. Lynn, Phys. Rev. B **69**, 054415 (2004).
[26] H. Kusunose, J. Phys. Soc. Jpn. **77**, 064710 (2008).
[27] T. Matsumura, T. Yonemura, K. Kunimori, M. Sera, and F. Iga, Phys. Rev. Lett. **103**, 017203 (2009).
[28] T. Nagao and J. I. Igarashi, Phys. Rev. B **82**, 024402 (2010).
[29] T. Matsumura, T. Yonemura, K. Kunimori, M. Sera, F. Iga, T. Nagao, and J. I. Igarashi, Phys. Rev. B **85**, 174417 (2012).
[30] R. Shiina, J. Phys. Soc. Jpn. **70**, 2746 (2001).
[31] R. Shiina, J. Phys. Soc. Jpn. **71**, 2257 (2002).
[32] K. Kubo and Y. Kuramoto, J. Phys. Soc. Jpn. **73**, 216 (2004).
[33] A. Kondo, H. Tou, M. Sera, and F. Iga, J. Phys. Soc. Jpn. **76**, 013701 (2007).
[34] F. Iga, N. Shimizu, and T. Takabatake, J. Magn. Magn. Mater. **177–181**, 337 (1998).
[35] C. Mazzoli, S. B. Wilkins, S. Di Matteo, B. Detlefs, C. Detlefs, V. Scagnoli, L. Paolasini, and P. Ghigna, Phys. Rev. B **76**, 195118 (2007).
[36] B. Detlefs, S. B. Wilkins, R. Caciuffo, J. A. Paixão, K. Kaneko, F. Honda, N. Metoki, N. Bernhoeft, J. Rebizant, and G. H. Lander, Phys. Rev. B **77**, 024425 (2008).
[37] T. Inami, S. Michimura, and T. Matsumura, J. Phys.: Conf. Ser. **425**, 132011 (2013).
[38] M. Hiroi, S. Kobayashi, M. Sera, N. Kobayashi, and S. Kunii, J. Phys. Soc. Jpn. **67**, 53 (1998).
[39] T. Nagao and J. I. Igarashi, Phys. Rev. B **74**, 104404 (2006).
[40] S. W. Lovesey, J. Fernández-Rodríguez, J. A. Blanco, and Y. Tanaka, Phys. Rev. B **75**, 054401 (2007).
[41] Y. Tanaka, K. Katsumata, S. Shimomura, and Y. Onuki, J. Phys. Soc. Jpn. **74**, 2201 (2005).
[42] T. Matsumura, T. Yonemura, K. Kunimori, M. Sera, and F. Iga, J. Phys. Soc. Jpn. **80**, SA054 (2011).
[43] K. Kunimori, M. Kotani, H. Funaki, H. Tanida, M. Sera, T. Matsumura, and F. Iga, J. Phys. Soc. Jpn. **80**, SA056 (2011).
[44] S. W. Lovesey and S. P. Collins, *X-ray Scattering and Absorption by Magnetic Materials* (Oxford University Press, New York, 1996).
[45] R. Shiina, H. Shiba, P. Thalmeier, A. Takahashi, and O. Sakai, J. Phys. Soc. Jpn. **72**, 1216 (2003).
[46] K. Iwasa, K. Kuwahara, M. Kohgi, P. Fisher, A. Donni, L. Keller, T. C. Hansen, S. Kunii, N. Metoki, Y. Koike, and K. Ohoyama, Physica B **329–333**, 582 (2003).
[47] O. Zaharko, P. Fischer, A. Schenck, S. Kunii, P.-J. Brown, F. Tasset, and T. Hansen, Phys. Rev. B **68**, 214401 (2003).
[48] P. Fischer, K. Iwasa, K. Kuwahara, M. Kohgi, and T. Hansen, and S. Kunii, Phys. Rev. B **72**, 014414 (2005).
[49] M. Sera and S. Kobayashi, J. Phys. Soc. Jpn. **68**, 1664 (1999).